Research Article ISSN 2832-9384

Journal of Materials and Polymer Science

Seeking Resonances in a $Al_yga_{1-y}AS/GaAs$ Nanostructure via Semiclassical Path Integration

Theodosios Geo. Douvropoulos

Hellenic Naval Academy, Sector of Natural Sciences: Pure & Applied Physics, Hatzikyriakou Ave. Piraeus, 18539, Greece.

***Corresponding Author**

Theodosios Geo. Douvropoulos
Hellenic Naval Academy, Sector of Natural Sciences: Pure & Applied Physics, Hatzikyriakou Ave. Piraeus, 18539, Greece.

Submitted : 16 Sept 2024 ; Published : 29 Nov 2024

Citation: Douvropoulos, T. G. (2024). Seeking Resonances in a $Al_yga_{1-y}AS/GaAs$ Nanostructure via Semiclassical Path Integration. J mate poly sci, 4(4) :1-10. DOI : https://doi.org/10.47485/2832-9384.1066

Abstract

In this paper, we conducted an analytical study of the resonant tunneling mechanism in an AlGaAs/GaAs heterostructure. Our focus was on developing a method to determine the resonance complex positions of the system using semiclassical path integration. To achieve this, we started by employing a one-dimensional effective model potential to describe the carrier's potential as it moves between layers. We then built the fixed energy amplitude of the structure by accounting for all changes in the phase of the carrier's wave-function as it propagated through infinite paths. The resonance positions were identified as complex poles of the overall amplitude. We discovered that these positions depend on both the geometric characteristics of the nanostructure, such as the well and barrier widths and the barrier height, and material properties like the aluminum's mole fraction. Our results provide clear analytical relationships and align with previously published findings, enabling us to predict and optimize the performance of various nanoscale devices.

Keywords: effective mass, heterostructure, lifetime, resonance, resonant tunneling, semiclassical path integration.

Introduction

Resonances in classical and quantum mechanics, refer to the case of maximum energy transfer. In classical mechanics, this happens when an external source's frequency matches the natural frequency of the system. In quantum mechanics, resonances have a complex spectrum due to the quantum tunneling effect (Kukulin et al., 2013). Resonant tunneling occurs when a quantum well is positioned between two quantum barriers, and maximum charge transport happens when the carrier's energy aligns with the discrete quantized levels of the quantum well (Ferry et al., 2001). However, the resonance position of the incoming carrier is shifted by a complex amount, where the imaginary part is equal to the inverse lifetime of the resonance state (Douvropoulos & Nicolaides, 2004; Nicolaides & Douvropoulos, 2005). This shift is related to the charge resonant transport time. It's important to note that there are pure classical systems that also exhibit a complex spectrum and a tunneling time (Douvropoulos, 2023).

The quantum tunneling effect is the dominant mechanism in resonance phenomena and was first observed in the thermionic emission of electrons from a metal surface (Fowler & Nordheim, 1928). When additional interfaces are involved, such as metal-metal or metal-semiconductor, other types of tunneling occur, such as interband, direct, phonon-assisted, coherent tunneling, and others (Ferry et al., 2001). Quantum confinement in atomic dimensions has evolved from a futuristic concept of the past to a present-day technological reality (Kim et al., 2020; Wu et al., 2022), enabling various applications in nanoelectronics and high-switching speed devices. In our current research, we are working with a double-barrier heterostructure, made from alternating GaAs and AlGaAs nanolayers. As a result, the effective potential that a carrier experiences changes only in the dimension vertical to the interface and can thus be treated as one-dimensional.

The current technology allows for precise control of both geometric and structural parameters of the heterostructure, opening up applications in photo conversion and photo catalysis, (Fang, et al., 2020; Tsao, et al., 2021; Yuan, et al., 2021; Wang, et al., 2023), optoelectronic devices, (Xie, et al., 2018; Yang & Hao, 2019; Tan, et al., 2021; Qiao, et al., 2022), photodetectors and phototransistors, (Su, et al., 2005 ; Xu, et al., 2017; Shin & Choi, 2018 ; Spies & Monroy, 2019 ; Li, et al., 2013) and spin-based devices (Spies & Monroy, 2019 ; Duy Khang & Hai, 2019; Xue, et al., 2021). Resonant tunneling in heterostructures is a topic of significant interest, with both experimental and theoretical studies being conducted. Experimental research includes the study of resonant tunneling of holes and electrons through Landau levels, (Mendez, et al., 1985; Mendez, et al., 1986), measurement of resonant

transport time in luminescence spectroscopic experiments (Alexander, et al., 1990), control of tunneling time with respect to dwell time (Mishchenko et al., 2014), and modification of the layer order or layer composition of the heterostructure to control the resonance peak (Lin, et al., 2015). Theoretical studies frequently employe the transfer matrix approach, Airy function formalism, complex energy method, and solution of transcendental equations to calculate resonance positions, transmission probability, and resonance positions and widths (Bahder, et al., 1987; Elabsy, 2000; Djelti, et al., 2014; Sattari, 2015; Rebey, et al., 2022; Elable & Attia, 2023).

While path integrals have been used to calculate various electron properties of the heterostructure, such as the density of states at the interface (Sa-yakanit & Slavcheva, 1998) and transport across the heterostructure with spin-orbit interactions (Bellucci & Onorato, 2010), they are not commonly used to calculate the resonance positions. In the past, the author calculated the fixed energy amplitude of a double-barrier heterostructure (Douvropoulos, 2014) via semiclassical path integration. However, the results were primarily qualitative and assumed a constant electron effective mass across the nanostructure. In this study, the system is modeled by assuming a linear effective potential resulting from the combination of the conduction band offset between the different layers and the application of a constant bias across the heterostructure. The Green's function is then constructed by taking into account the phase changes of the electron's wave function due to propagation or reflection using the semiclassical path integral theory. In this way, the geometric characteristics of the system, such as the width of the effective well and barriers, as well as structural characteristics such as the mass mismatch and the applied bias, strongly influence the calculation of the resonance positions.

In the following section, we will create the effective potential that corresponds to the motion of the electron within the heterostructure. We will then introduce the semiclassical path integration technique and use it to develop the system's Green's function. The resonance positions will be determined as the complex poles of the fractional Green's function. We will examine how the resonance positions depend on the applied bias, the mole fraction of Aluminum, and the geometric characteristics of the system. Our findings will be presented through a variety of graphs. To conclude, we will summarize our results and provide a brief conclusion.

Materials

When an AlGaAs layer follows a GaAs layer, a barrier is created due to the energy difference in the conduction bands of the two layers. This difference is known as the conduction band offset (Hanson, 2019), which is equal to the barrier height and depends on the concentration of Aluminum. A double barrier potential can be created by the sequence of AlGaAs/GaAs/AlGaAs, where two AlGaAs layers are grown epitaxially to form the barriers using modern crystal techniques (Kim, et al., 2020; Wu, et al., 2022). The resonance state is one of the quantized levels of the GaAs well. This is illustrated in Figure 1, which also shows two heavily doped GaAs regions positioned to the left and right of the aforementioned sequence. These heavily doped regions are usually referred to as the emitter and the collector, describing the departure and arrival of the carrier, respectively. Their maximum occupied energy level corresponds to the Fermi energy.

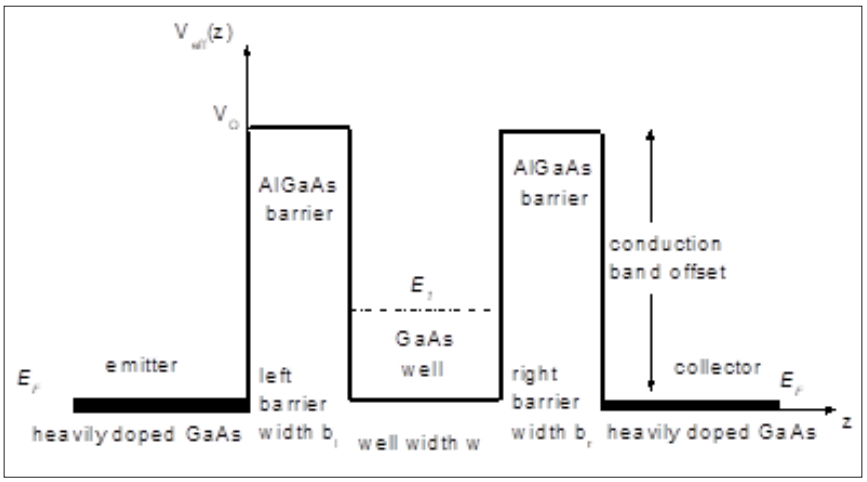

Figure 1: An effective double barrier potential $V_{eff}(z)$ is created due to the difference in the conduction bands of the GaAs and AlGaAs layers. The material changes in the z direction. The in-between GaAs well is quantized and then E_1 is the lowest quantum level (resonance) of the well. The barrier height V_O is due to the conduction band offset, while E_f refers to the Fermi level of the heavily doped GaAs layers.

The mole fraction of aluminium, denoted as y, determines various material properties of the heterostructure. For electrons, y determines their effective mass, which is a measure of the carrier's inertia. This simplifies the complexity of the band structure, as it corresponds to the same dynamics but with a free particle of that mass instead (Pereyra, 2019). The effective mass, denoted as μ*, is defined as inversely proportional to the second-order derivative of electron energy with respect to wave number according to the following expression:

$$\mu^* = \hbar^2 \left(\frac{\partial^2 E}{\partial k^2} \right)^{-1} \quad (1)$$

Each layer is assumed to have a constant effective mass that changes non-continuously as we move from one layer to another. For the GaAs well, the electron effective mass is typically taken as $\mu^*_w = 0.067$me (where me is the mass of a free electron). However, for the $Al_yGa_{1-y}As$ barrier, the effective mass varies linearly with the mole fraction of aluminum y as $\mu^*_b(y) = (0.067 + 0.083y)\, m_e$ (Hanson, 2019).

The energy gap between the conduction and valence band of the $Al_yGa_{1-y}As$ layer with Aluminum's mole fraction is described by the linear relation: Eg=1.426+1.247y. Here, 1.426 eV represents the energy gap of GaAs at room temperature (300 K) (Hanson, 2019). Additionally, the barrier height of the $Al_yGa_{1-y}As$ layer in Figure 1 depends on y, and this relationship is more complex with various proposed models for defining the conduction band offset. One simple approximation is the 60-65% rule, which defines the conduction band offset as 60-65% of the difference in the energy gaps of the AlyGa1-yAs and GaAs layers (Adachi, 1985). However, our current semi-classical analysis considers the semi-local exchange potential method more consistent for calculating the band gaps of the interface (Wang, et al., 2013), where the barrier height varies linearly with mole fraction y as:

$$V_O = 0.243 + 0.36(y - 0.3) \quad in\ eV, for \quad 0.3 \le y \le 0.4 \qquad (2)$$

Resonant tunneling occurs when the energy of the incoming electron matches one of the quantized levels of the GaAs well, leading to maximum flow across the heterostructure. We can induce resonant tunneling by applying a constant bias between the emitter and the collector, as shown in the following Figure 2.

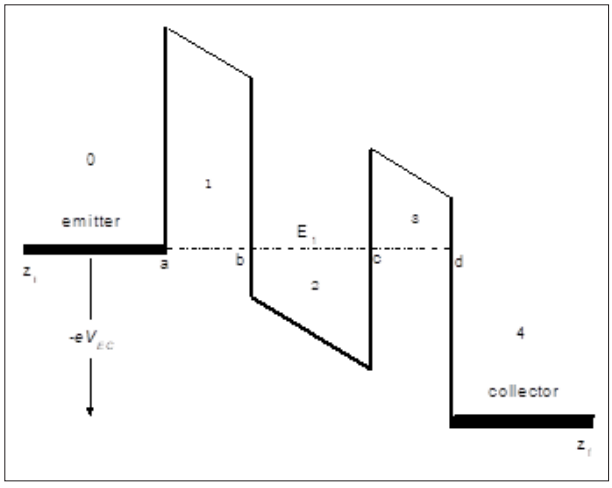

Figure 2: When a constant bias (V_{EC}) is applied between the collector and the emitter, the quasi-bound state E_1 is lowered to the Fermi level of the left contact, generating resonant tunneling. The potential becomes approximately linear. There are three regions of motion (1,2,3) and four turning points (a,b,c,d), while z_i and z_f stand for the initial and final point of charge transport.

In the figure above, the applied bias is uniformly distributed across the heterostructure, making the effective potential linear with space. The bias not only changes the potential slope and shape, but also affects the height of the barriers. These perturb the quantized levels of the well, causing the lowest level E_1 to approach the Fermi level of the left contact, which generates resonant tunneling. Electrons from the collector face a large barrier preventing them from tunneling to the left contact. However, when the applied bias is increased further, the resonance level E_1 drops below the Fermi level of the emitter, leading to decreased flow and the negative differential resistance phenomenon. Resonant tunneling occurs again when the first excited resonance state of the well, E_2, is lowered to align with the conduction band of the emitter.

The linearity of the effective potential of Figure 2 is approximately true. The main source of non-linearity is the electron-electron interaction (Meghoufel, 2013). However, introducing the electron effective mass model makes the contribution of the non-linear terms less significant, as the electron is treated as a free particle.

Methods

The spectrum of the heterostructure can be calculated by solving the Schrödinger equation numerically in a self-consistent mode (Farnam, et al., 2019). Another approach is to construct the system's Green's function and identify the spectrum as the set of complex poles of its fractional part [1]. The semi-classical path integral formalism is based on Gutzwiller's periodic orbit theory (Gutzwiller, 1971) to construct the system's Green's function, considering quadratic corrections around the classical propagation path. By assuming a specific energy value, we can Fourier transform the Green's function to the time domain and analytically continue the propagator including paths of imaginary times (Holstein & Swift, 1982). By transforming back to the energy domain, we can construct the fixed energy amplitude, with each possible path contributing through a set of change factors corresponding to the change of the electron's wave function due to propagation or reflection.

The above procedure can be encapsulated in the following formula that describes the overall contribution for propagation between endpoints z_i and z_f of the heavily doped GaAs layers (Holstein & Swift, 1982):

$$G_{sc}(E) = \frac{\sqrt{\mu^*}}{2\pi\hbar\left(2\sqrt{E - V_{eff}(z_i)}\sqrt{E - V_{eff}(z_f)}\right)^{1/2}} \sum_{\kappa=1}^{\infty}\left\{\prod_{i=1}^{N(\kappa)}\left({}^{i}\lambda^{\kappa}\right)\right\} \qquad (3)$$

In this formula, we obtain an infinite sum of products formed by various combinations of change factors $\left({}^{i}\lambda^{\kappa}\right)$, each representing a specific path. These paths are infinite in number, and the change factors can be categorized into propagation and reflection types. Their analytic definitions are included in Table 1:

PROPAGATION CHANGE FACTORS $\left({}^{i}\lambda^{\kappa}\right)$ Turning Points (a, b, c, d)	REFLECTION CHANGE FACTORS $\left({}^{i}\lambda^{\kappa}\right)$		
POTENTIAL WELL: $\exp\left\{i\int_{b}^{c}\sqrt{2\mu_{w}^{*}\left(E-V_{eff}(z)\right)}/\hbar dz\right\}\equiv e^{i\cup}$	BACK TO THE WELL	BACK TO THE BARRIER	FROM AN INFINITE BARRIER
	$-i\sqrt{\frac{\mu_{b}^{*}}{\mu_{w}^{*}}}$	$\frac{i}{2}\sqrt{\frac{\mu_{w}^{*}}{\mu_{b}^{*}}}$	-1
POTENTIAL BARRIER: $\exp\left\{-\left\|\int_{a/c}^{b/d}\sqrt{2\mu_{b}^{*}\left(V_{eff}(z)-E\right)}/\hbar dz\right\|\right\}\equiv e^{-\cap_{L/R}}$	E is the particle's energy, and $V_{eff}(z)$ the effective potential function.		

Table 1: Definition of the change factors for propagation and reflection from the turning points.

The parameter μ* represents the electron's 'effective mass' within the propagation region of the two endpoints z_i and z_f. This is distinct from μ^*_w and μ^*_b which denote the effective masses within the GaAs well and the AlGaAs barriers, respectively. E represents the incoming electron's energy, while $V_{eff}(z)$ corresponds to the effective linear potential function.

In accordance with Figure 2, the heterostructure is divided into three classically allowed regions of motion (0, 2, 4) and two classically forbidden regions (1 and 3). Our task is to calculate the total fixed energy amplitude connecting z_i and z_f in every possible way. To achieve this, we need to break down the problem into smaller parts. To start, we define the zeroth order amplitude as the one that directly connects two points in a straight path. Then, the first order amplitude involves propagation between two points with the path repeating itself in all possible ways, including multiple reflections. The second-order amplitude involves the interchange of two regions of motion that connect two space points, and can be expressed as a function of simpler first-order amplitudes. Finally, the third-order amplitude combines three regions of motion for propagation between two space points, and is a function of simpler second-order amplitudes.

- When traveling from the starting point z_i to the first turning point a, there is a single straight path in the classically forbidden region 0, making it a zeroth order amplitude. This path does not include any reflections or repetitions. Referring to Table 1, the amplitude can be represented as shown in the following equation

$$T_0^{z_i\to a}=\exp\left[\frac{i}{\hbar}\sqrt{2\mu^{*}E}(a-z_i)\right] \qquad (4)$$

The upper indices of the amplitude represent the two endpoints of propagation connected with a single arrow, while the lower index corresponds to the region of motion.

- The next option involves traveling from turning point a to turning point c through regions 1 and 2 only. In this case, we need to interchange regions 1 and 2 in all possible ways, resulting in the second-order amplitude $\left(1\rightleftharpoons 2\right)^{a}_{c}$. The upper indices of the amplitude represent the endpoints of propagation for each region, with the two arrows of different directions express the interchange of the two regions with the longer one pointing to the final propagation region. This second-order amplitude can be expressed as a function of simpler first-order amplitudes, as defined above. Thus,

$$\left(1\rightleftharpoons 2\right)^{a}_{c}=T_1^{a\rightleftarrows b}\,T_2^{b\rightleftarrows c}+T_1^{a\rightleftarrows b}\,T_2^{b\rightleftarrows c}\left(-i\sqrt{\frac{\mu_b^*}{\mu_w^*}}\right)e^{i\cup}\,T_1^{b\rightleftarrows b}\,T_2^{b\rightleftarrows c}+\ldots$$

$$=\frac{\sqrt{\mu_w^*}\,T_1^{a\rightleftarrows b}\,T_2^{b\rightleftarrows c}}{\sqrt{\mu_w^*}+i\sqrt{\mu_b^*}e^{i\cup}\,T_1^{b\rightleftarrows b}\,T_2^{b\rightleftarrows c}} \qquad (5)$$

The two-way arrow, first order amplitudes in the formula above correspond to the various pathways connecting the two endpoints in both directions. For example, the ${}^{a}T_1^{b}$ amplitude describes the sum of all (infinite) paths connecting points a and b by travelling exclusively inside region 1. These pathways form a geometric progression due to self repetition, which is then summed up in the compact formula provided.

- We have two options to consider: either combining regions 3 and 2, excluding region 1, or combining all three regions (3, 2, 1) to reach point c.

refers to the infinite interchange of regions 3 and 2 in all possible ways. We symbolize this as

$$\left(3\rightleftharpoons 2\right)^{c}_{c} \qquad (6)$$

Its calculation is similar to that of $\left(1\rightleftharpoons 2\right)^{a}_{c}$, and the result will be provided in the Table 2 that follows.

refers to traveling from point c back to point c through the combination of all three regions (1, 2, 3) in every possible way. The possible partial interchanges always come in pairs, and the last pair is naturally the combination of regions 1 and 2. This is a third-order amplitude and is expressed as the following function.

$$\left\{\left(3\rightleftharpoons 2\right)^{c}_{b}\rightleftharpoons\left(1\rightleftharpoons 2\right)^{b}_{c}\right\}\rightleftharpoons\left\{1+\left(3\rightleftharpoons 2\right)^{c}_{c}\right\} \qquad (7)$$

The overall contribution for propagation from point c back to c through all three regions is equal to the sum of the distinguished cases

$$\underset{1,2,3}{\overset{c\circlearrowright c}{A}} = \frac{\left\{1+\left(\overset{c}{3}\rightleftharpoons\overset{c}{2}\right)\right\}}{1-\left\{\left(\overset{c}{3}\rightleftharpoons\overset{b}{2}\right)\left(\overset{b}{1}\rightleftharpoons\overset{c}{2}\right)\right\}} \tag{8}$$

With only region 3 remaining for our paths, there is a final propagation within region 3 traveling from point c to d. This final propagation is the first-order amplitude ${}^{a}T_{1}{}^{b}$, which can be calculated as follows:

$$\overset{c\rightleftarrows d}{T_3} = e^{-\curvearrowright_R} - e^{-\curvearrowright_R}\frac{\mu_w^* e^{-2\curvearrowright_R}}{4\mu_b^*} + .. = \frac{1}{e^{\curvearrowright_R} + \mu_w^* e^{-\curvearrowright_R}/4\mu_b^*} \tag{9}$$

At the end, there is only left a single propagation from d to z_f inside region 4 of the collector, which is the zeroth amplitude $\overset{a\rightleftarrows b}{T_1}$ calculated as follows

$$\overset{d\rightarrow z_f}{T_4} = \exp\left[\frac{i}{\hbar}\sqrt{2\mu^*(E+eV_{CE})}(z_f-d)\right] \tag{10}$$

In Table 2 that follows, we have calculated all the second order amplitudes that are involved in the propagation, in terms of the simpler first order amplitudes.

$\left(\overset{a}{1}\square\overset{c}{2}\right)$	$\frac{\sqrt{\mu_w^*}\,\overset{a\square b}{T_1}\,\overset{b\square c}{T_2}}{\sqrt{\mu_w^*}+i\sqrt{\mu_b^*}e^{i\backsim}\,\overset{b\square b}{T_1}\,\overset{b\square c}{T_2}}$
$\left(\overset{b}{1}\square\overset{c}{2}\right)$	$\frac{\overset{b\square b}{T_1}\,\overset{b\square c}{T_2}}{1-\overset{b\square b}{T_1}\,\overset{b\square b}{T_2}}$
$\left(\overset{c}{3}\square\overset{c}{2}\right)$	$\frac{\overset{c\square c}{T_3}\,\overset{c\square c}{T_2}}{1-\overset{c\square c}{T_3}\,\overset{c\square b}{T_2}}$
$\left(\overset{c}{3}\square\overset{b}{2}\right)$	$\frac{\overset{c\square c}{T_3}\,\overset{c\square b}{T_2}}{1-\overset{c\square c}{T_3}\,\overset{c\square c}{T_2}}$

Table 2: Calculation of the second order amplitudes in terms of first order amplitudes.

In Table 3 that follows, we have calculated the first order amplitudes of the above table as a function of the fundamental change factors that appear in Table 1:

$\overset{a\square b}{T_1}$	$\left(e^{\curvearrowright_L}+\frac{\mu_w^* e^{-\curvearrowright_L}}{4\mu_b^*}\right)^{-1}$
$\overset{b\square b}{T_1}$	$i\left(2e^{2\curvearrowright_L}\frac{\sqrt{\mu_b^*}}{\sqrt{\mu_w^*}}+\frac{\sqrt{\mu_w^*}}{2\sqrt{\mu_b^*}}\right)^{-1}$
$\overset{b\square c}{T_2}$	$\mu_w^*\left(\mu_b^* e^{i\backsim}+\mu_w^* e^{-i\backsim}\right)^{-1}$
$\overset{c\square c}{T_2}$	$\frac{-i\sqrt{\mu_w^*\mu_b^*}}{\mu_b^*+\mu_w^* e^{-2i\backsim}}$
$\overset{c\square d}{T_3}$	$\left(e^{\curvearrowright_L}+\frac{\mu_w^* e^{-\curvearrowright_R}}{4\mu_b^*}\right)^{-1}$
$\overset{c\square c}{T_3}$	$i\left(2e^{2\curvearrowright_R}\frac{\sqrt{\mu_b^*}}{\sqrt{\mu_w^*}}+\frac{\sqrt{\mu_w^*}}{2\sqrt{\mu_b^*}}\right)^{-1}$

Table 3: First order amplitudes involved in the propagation as a function of the fundamerntal change factors that are included in Table 1

By combining the previous equations and carefully performing the tedious calculations, we finally express the overall Green's function of equation (3) in terms of the fundamental change factors of Table 1 and get the following formula:

$$G_{sc}(E) = \frac{\sqrt{\mu^*}}{2\pi\hbar\left(2\sqrt{E-V_{eff}(z_i)}\sqrt{E-V_{eff}(z_f)}\right)^{1/2}} \sum_{K=1}^{\infty}\left\{\prod_{i-1}^{N(\kappa)}\left(i\lambda^{\kappa}\right)\right\}$$

$$G_{sc}(E) = \frac{\sqrt{\mu^*}}{2\pi\hbar\left(2\sqrt{E-V_{eff}(z_i)}\sqrt{E-V_{eff}(z_f)}\right)^{1/2}} \overset{z_i\to a}{T_0}\left(\overset{a}{1}\rightleftharpoons\overset{c}{2}\right)\frac{1+\left(\overset{c}{3}\rightleftharpoons\overset{c}{2}\right)}{1-\left(\overset{c}{3}\rightleftharpoons\overset{b}{2}\right)\left(\overset{b}{1}\rightleftharpoons\overset{c}{2}\right)} \overset{c\rightleftharpoons d}{T_3}\overset{d\to z_f}{T_4} =$$

$$\frac{8\sqrt{2}(\mu^*\mu_w^*)^{1/2}}{\sqrt{\mu_b^*}\pi\hbar\left(E(E+eV_{EC})\right)^{1/4}} \times \frac{\exp\left[\frac{i}{\hbar}\sqrt{2\mu^* E}(a-z_i)\right]}{\left(4\sqrt{\frac{\mu_b^*}{\mu_w^*}}e^{\cap_L}+\sqrt{\frac{\mu_w^*}{\mu_b^*}}e^{-\cap_L}\right)} \frac{\exp\left[\frac{i}{\hbar}\sqrt{2\mu^*(E+eV_{EC})}(z_f-d)\right]}{\left(4\sqrt{\frac{\mu_b^*}{\mu_w^*}}e^{\cap_R}+\sqrt{\frac{\mu_w^*}{\mu_b^*}}e^{-\cap_R}\right)}$$

$$\frac{}{\left(1+\frac{\left(\mu_w^*\right)^2 e^{-2(\cap_L+\cap_R)}}{8\left(\mu_b^*\right)^2}-\frac{\mu_w^*}{\mu_b^*}\frac{e^{-2\cap_L}+e^{-2\cap_R}}{4}\right)\left(\sqrt{\frac{\mu_b^*}{\mu_w^*}}e^{i\cup}+\sqrt{\frac{\mu_w^*}{\mu_b^*}}e^{-i\cup}\right)+\left(\frac{\left(\mu_w^*\right)^2 e^{-2(\cap_L+\cap_R)}}{8\left(\mu_b^*\right)^2}-\frac{\mu_w^*}{\mu_b^*}\frac{e^{-2\cap_L}+e^{-2\cap_R}}{4}\right)\left(\sqrt{\frac{\mu_b^*}{\mu_w^*}}e^{i\cup}-\sqrt{\frac{\mu_w^*}{\mu_b^*}}e^{-i\cup}\right)} \quad (11)$$

Results and Discussions

The Green's function of the heterostructure reveals the complex spectrum of the system, represented by the complex poles of its fractional part. When quantum tunneling is involved, the poles acquire an imaginary part, influencing the system's evolution (Douvropoulos & Nicolaides, 2003). In equation (11), the maximum value is achieved when the energy coincides with one of the resonance positions, indicated by the nullification of the denominator.

To calculate the complex resonance positions, we can expand the denominator around the real eigenvalues of the quantum well, which correspond to its dominant contribution. The amplitude of Table 3 corresponds to the propagation inside the quantum well. We aim to explore its relationship with the energy eigenvalues of the quantum well. Assuming the GaAs quantum well has infinite walls (an approximation true as long as the barrier height significantly outweighs its lower eigenstate due to the large enough mole fraction of Aluminium), the reflection factor (as shown in Table 1) is calculated to be -1 and the amplitude can be calculated as follows.

$$\overset{c\rightleftharpoons c}{T_2} = e^{-i\cup}(-1)e^{-i\cup}(-1)+\left\{e^{-i\cup}(-1)e^{-i\cup}(-1)\right\}^2+..$$

$$=\frac{e^{-2i\cup}}{1-e^{-2i\cup}}=\frac{e^{-i\cup}}{e^{i\cup}-e^{-i\cup}}=\frac{e^{-i\cup}}{2i\sin\cup} \quad (12)$$

The nullification of the sinus term in the above formula provides the condition for the eigenvalues of the infinite well:

$$\sin\cup=0\Rightarrow\cup=n\pi\Rightarrow\left(\sqrt{2\mu_w^*}/\hbar\right)\int_b^c\sqrt{E}dz=n\pi\Rightarrow$$

$$\left(\sqrt{2\mu_w^*}/\hbar\right)\sqrt{E}\left(c-b\right)=n\pi\Rightarrow E=n^2\frac{\hbar^2\pi^2}{2\mu_w^*\left(c-b\right)^2} \quad (13)$$

Similarly, when the denominator of the $\overset{c\rightleftharpoons c}{T_2}$ amplitude is nullified, it reveals the quantized levels of the quantum well. In equation (11), the dominant contribution in the denominator of the overall Green's function comes from the real part of the eigenvalues of the GaAs well. Our calculations were conducted for the unbiased potential shown in Figure 1 for simplicity. When a constant bias is applied, the effective potential changes according to Figure 2. The $\overset{c\rightleftharpoons c}{T_2}$ amplitude still represents the condition for maximum contribution, which now reads:

$$\mu_b^*\cos\left(2\cup\right)+\mu_w^*=0 \quad (14)$$

The condition mentioned above is used to extract the real part of the resonance positions. To find the complex shift, we develop the denominator of the Green's function in equation (11) around these real parts. We consider two cases (I and II) by changing the widths of the neighboring AlGaAs barrier to the emitter and the GaAs well. The geometric characteristics of the heterostructure, listed in the following Table 4, are chosen to facilitate comparison with existing literature on the subject.

Heterostructure	α(nm)	β(nm)	γ (nm)	δ (nm)
I	0	1.5	3.5	5.0
II	0	1.0	3.5	5.0

Table 4: The heterostructure dimensions, for the two cases under study.

We then calculate the resonance positions using condition (14) for five different values of the applied bias for both I and II structures. Our results, obtained for Aluminum's mole fraction of y=0.34, are in excellent agreement with previous publications (Merghoufel, 2013).

Applied Bias (V)	0.001	0.050	0.100	0.150	0.200
I Resonance Position (eV)	0.196	0.171	0.146	0.121	0.097
II Resonance Position (eV)	0.125	0.103	0.081	0.059	0.037

Table 5: The lowest resonance energy position, for the two types of heterostructure, I and II, for five different values of the applied bias.

In the next step, we will calculate the lowest resonance position (E_1) based on the applied bias for both types of the GaAs/AlGaAs heterostructure. These calculations will be conducted

using the geometric characteristics specified in Table 2, and assuming that the electron's effective mass inside the barrier is 1.458 times the electron's effective mass inside the well. The applied bias will impact the slope of the potential, while the electron's effective mass will determine the barrier height. Our findings will be presented in Figure 3. Specifically, they show a nearly linear decrease with the applied bias, which aligns with previous literature (Terkhi, et al., 2012; Merghoufel, 2013; Elabsy & Attia, 2023).

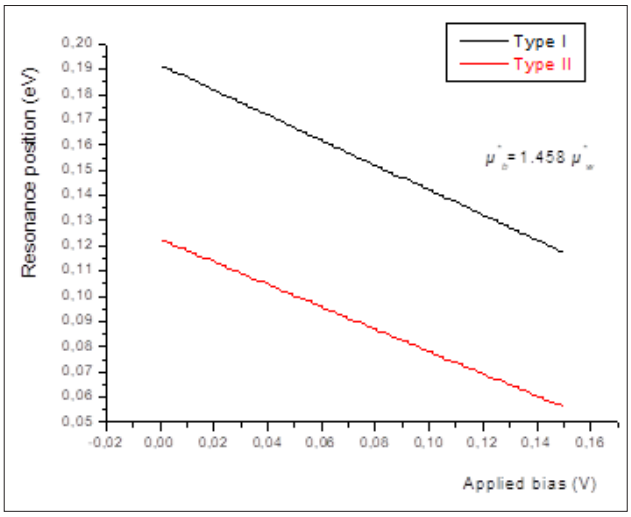

Figure 3: The dependence of the lowest resonance state on the applied bias, for both types of the heterostructure (I, II). The calculations are carried out for an electron effective mass inside the AlGaAs barrier equal to 1.458 times the electron effective mass inside the GaAs well.

Furthermore, as shown in Figure 3, the resonance position of type II hetero-structure is lower than that of type I for all values of the applied bias. This is consistent with the laws of quantum mechanics, as type II has a wider width and therefore supports lower energies. This can be easily understood from expression (13) and the uncertainty principle as well. We can gain further insight into the properties of resonance position by studying its dependence on the electron-effective mass within the barrier. This mass indicates the electron's inertia. In the following Figure 3, we illustrate the lowest resonance energy as a function of for two different values of the applied bias for both type I and type II.

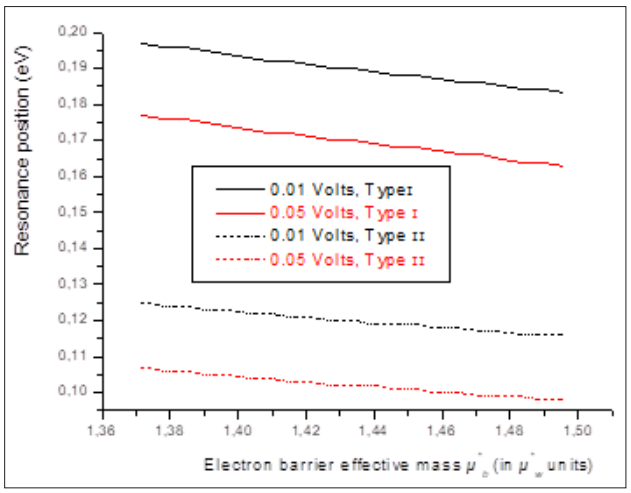

Figure 4: The resonance position as a function of the electron's effective mass inside the AlGaAs barrier. The solid lines represent the type I heterostructure, while the dashed and dotted lines represent type II. The results indicate a gradual decrease with and the applied bias. The decrease is more pronounced when the width of GaAs is increased (type II).

According to Figure 4, the resonance position decreases not only with the applied bias, but also with the electron-effective mass inside the AlGaAs barrier. This is due to the laws of quantum mechanics, as the GaAs well becomes deeper and can support lower energy levels. When the width of the GaAs is increased (type II heterostructure), the resonance positions become lower, in agreement with the quantum laws (see eq. (13)) and the uncertainty principle. The complex shift of the resonance, relative to its unperturbed value, is revealed when we develop the complex denominator of the Green's function in (11) around the lowest resonance positions found in Table 3. Hence, we calculate the complex resonance positions, including both the real energy shift and the width, as follows:

$$E_R \cong \left(E_o + \frac{\alpha\delta - \beta\gamma}{\gamma^2 + \delta^2}\right) + \frac{i}{2}\frac{2\alpha\gamma + 2\beta\delta}{\gamma^2 + \delta^2} \equiv E_o + \Delta E_r - i\frac{\Gamma}{2} \tag{15}$$

$$\alpha = \left(e^{-2\cap_L} + e^{-2\cap_R}\right), \beta = \frac{e^{-2(\cap_L + \cap_R)}}{4},$$

$$\gamma = -\frac{e^{-2(\cap_L+\cap_R)}}{4}\left(\frac{d\cup}{dE}\bigg|_{E_o} + 2\left(\frac{d\cap_L}{dE}\bigg|_{E_o} + \frac{d\cap_R}{dE}\bigg|_{E_o}\right)\right) - 4\frac{d\cup}{dE}\bigg|_{E_o} \tag{16}$$

$$\delta = 2\left(e^{-2\cap_L}\frac{d\cap_L}{dE}\bigg|_{E_o} + e^{-2\cap_R}\frac{d\cap_R}{dE}\bigg|_{E_o}\right)$$

The formula presented considers ER as the complex resonance position, which includes the real energy shift ΔEr and the width Γ. The width represents the full width for half maximum (FWHM) in the case of a Breit-Wigner energy distribution (Douvropoulos & Nicolaides, 2004). Therefore, the transport time for the carrier at resonance is connected to the lifetime of the resonance state, assuming an exponential decay law for the system's evolution. The resonant transport time is directly linked to the resonance width through equation

$$\tau_{res} = \hbar / \Gamma \tag{17}$$

and with reference to (13,14), we can express the resonant transport time as follows.

$$\tau_{res} = -\frac{\hbar}{2}\frac{\gamma^2 + \delta^2}{a\gamma + \beta\delta} \qquad (18)$$

Formula (18) represents the resonant transport time of the heterostructure when we consider other time scales, like the capacitance time scale or the transit time scale across the non-tunneling regions [6], to be insignificant. In current manufacturing practices, this assumption holds true when the heterostructure is properly designed. Our findings indicate a nearly linear increase in transport time with the electron effective mass inside the AlGaAs barrier, for mole fraction values of Aluminium ranging from 0.3 to 0.4. This aligns with existing literature on the subject (Wang, et al., 2006; Merghufel, et al., 2013; Elabsy & Attia, 2023). Figure 5 illustrates the aforementioned dependence

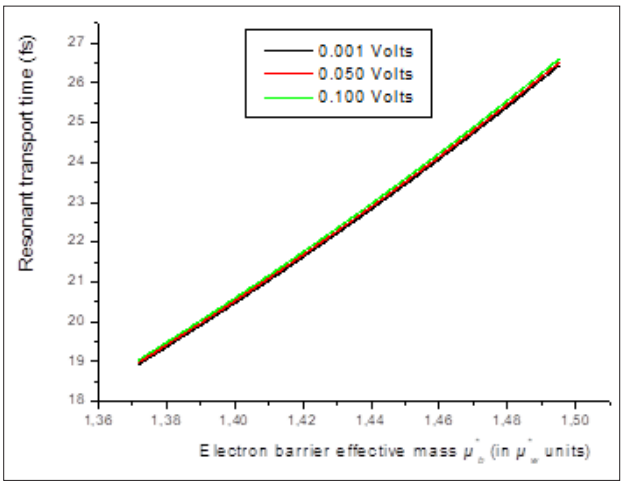

Figure 5: Resonant transport time seems to increase almost in a straight line as the electron's effective mass changes within the AlGaAs barrier. We conducted our calculations using a barrier width of 0.5 nm and a GaAs well width of 4 nm, at three different applied bias values. Interestingly, we found that the transport time remains the same regardless of the applied bias, as the three lines overlap.

Increasing the effective mass of the electron inside the barrier results in longer lifetimes. This is because, according to equation (2), the barrier height increases with the electron's effective mass. As a result, the electron encounters a higher barrier, making it more difficult to escape to the collector. This causes the electron to spend more time inside the GaAs quantum well. Additionally, the transport time appears to be independent of the applied bias. According to Figure 5, it is apparent that all three lines tend to coincide, even when they correspond to applied biases that differ by two orders of magnitude. This is consistent with existing literature (Elabsy & Attia, 2023) and indicates the increased inertia experienced by the carrier as it moves within the heterostructure. Furthermore, the resonant transport time is nearly independent of the applied bias, which also aligns with existing literature (Wang, et al., 2006; Elabsy & Attia, 2023). In terms of the time scale in Figure 5, it should be noted that the nanostructure-based device will operate within the frequency range of 35 to 50 THz.

Conclusion

In our research, we developed a method for determining the resonance positions in a double barrier $Al_yGa_{1-y}As$/GaAs heterostructure, focusing on electron transport between heavily doped GaAs layers serving as the emitter and the collector. We created a model of the structure using an effective one-dimensional potential with different electron-effective masses for the barriers and the well. Additionally, we applied a constant bias along the heterostructure to achieve resonant tunneling conditions. We utilized the semiclassical path integral formalism to construct the system's Green's function and derived an analytic formula. The resonance positions were identified as the complex poles of the Green's function fractional part. Our calculated lowest resonance positions closely matched previously published results. We observed that the resonance positions decrease with both the applied bias and the GaAs width, consistent with the principles of quantum mechanics as reported in existing literature. Furthermore, we found that the resonance positions decrease with the electron's effective mass inside the barrier, with the barrier height being directly proportional to the effective mass. Consequently, an increase in the effective mass results in a deeper GaAs well, supporting lower energy levels in accordance with quantum mechanics. However, the resonant transport time increases almost linearly with the effective mass and is independent of the applied bias for the same reasons. Specifically, for aluminium concentrations between 0.3 and 0.4, the transport time is on the order of a few femtoseconds, defining the operational range of the studied heterostructure in the THz region. Our results align well with existing literature.

Conflicts of Interest

The author declares no competing interests.

ORCID ID

T G Douropoulos https://orcid.org/0000-0003-4574-0507

References

1. Kukulin, V. I., Krasnopolsky, V. M., & Horácek, J. (2013). Theory of resonances: Principles and Applications, (Vol. 3). Berlin: Springer Science & Business Media. https://play.google.com/store/books/details/Theory_of_Resonances_Principles_and_Applications?id=vHfoCAAAQBAJ&hl=en_IN
2. Ferry, D., Bird, J. & Goodnick, S. M. (2001). Transport in Nanostructures (2nd ed.). Cambridge University Press. https://assets.cambridge.org/97805218/77480/frontmatter/9780521877480_frontmatter.pdf
3. Douvropoulos, T. G., & Nicolaides, C. A. (2004). Nonexponential decay propagator and its differential equation for real and complex energy distributions of unstable states. *Physical Review A, 69*(3), 032105. https://journals.aps.org/pra/abstract/10.1103/PhysRevA.69.032105

4. Nicolaides, C. A., & Douvropoulos, T. G. (2005). Shape resonances as poles of the semiclassical Green's function obtained from path-integral theory: Application to the autodissociation of the He2++ Σg+ 1 state. *The Journal of chemical physics, 123*(2) 024309. DOI: https://doi.org/10.1063/1.1961487
5. Douvropoulos, T. G. (2023). Semiclassical calculation of the pendulum period. *European Journal of Physics, 44*(6), 065803. DOI: http://dx.doi.org/10.1088/1361-6404/acf81d
6. Fowler, R. H., & Nordheim, L. (1928). Electron emission in intense electric fields. *Proceedings of the Royal Society of London. Series A, Containing Papers of a Mathematical and Physical Character, 119*(781), 173-181. https://ivanik3.narod.ru/Termojad/Gorjachiy/PRSLA-1928-Fowler-173-81.pdf
7. Kim, T., Fan, S., Lee, S., Joo, M. K., & Lee, Y. H. (2020). High-mobility junction field-effect transistor via graphene/MoS2 heterointerface. *Scientific reports, 10*(1), 13101. DOI: https://doi.org/10.1038/s41598-020-70038-6
8. Wu, F., Tian, H., Shen, Y., Hou, Z., Ren, J., Gou, G., Sun, Y., Yang, Y., & Ren, T. L. (2022). Vertical MoS2 transistors with sub-1-nm gate lengths. *Nature, 603*(7900), 259-264. DOI: https://doi.org/10.1038/s41586-021-04323-3
9. Fang, M. J., Tsao, C. W., & Hsu, Y. J. (2020). Semiconductor nanoheterostructures for photoconversion applications. Journal of Physics D: *Applied Physics, 53*(14), 143001. https://iopscience.iop.org/article/10.1088/1361-6463/ab5f25/meta
10. Tsao, C. W., Fang, M. J., & Hsu, Y. J. (2021) Modulation of interfacial charge dynamics of semiconductor heterostructures for advanced photocatalytic applications. Coord. *Chem. Rev.,* 438, 213876. DOI: https://doi.org/10.1016/j.ccr.2021.213876
11. Yuan, L., Geng, Z., Xu, J., Guo, F., & Han, C. (2021). Metal-Semiconductor Heterostructures for Photoredox Catalysis: Where Are We Now and Where Do We Go?. *Advanced Functional Materials, 31*(27), 2101103. DOI: https://doi.org/10.1002/adfm.202101103
12. Wang, S., Liao, W., Su, H., Pang, S., Yang, C., Fu, Y., & Zhang, Y. (2023). Review on the application of semiconductor heterostructures in photocatalytic hydrogen evolution: state-of-the-art and outlook. *Energy & Fuels, 37*(3), 1633-1656. DOI: http://dx.doi.org/10.1021/acs.energyfuels.2c03429
13. Xie, C., Wang, Y., Zhang, Z. X., Wang, D., & Luo, L. B. (2018). Graphene/semiconductor hybrid heterostructures for optoelectronic device applications. *Nano Today*, 19, 41-83. DOI: http://dx.doi.org/10.1016/j.nantod.2018.02.009
14. Yang, Z., & Hao, J. (2019). Recent progress in 2D layered III–VI semiconductors and their heterostructures for optoelectronic device applications. *Advanced Materials Technologies, 4*(8), 1900108. DOI: https://doi.org/10.1002/admt.201900108
15. Tan, J., Li, S., Liu, B., & Cheng, H. M. (2021). Structure, preparation, and applications of 2D material-based metal–semiconductor heterostructures. *Small Structures, 2*(1), 2000093. DOI: https://doi.org/10.1002/sstr.202000093
16. Qiao, P., Xia, J., Li, X., Ru, F., Liu, P., Tian, L., Jiang, X., Lin, Z., Chen, X. & Meng, X. M. (2022). Edge-Assisted Epitaxy of 2D TaSe2-MoSe2 Metal–Semiconductor Heterostructures and Application to Schottky Diodes. *Advanced Functional Materials, 32*(30), 2201449. DOI: https://doi.org/10.1002/adfm.202201449
17. Su, X., Chakrabarti, S., Bhattacharya, P., Ariyawansa, G., & Perera, A. G. U. (2005). A resonant tunneling quantum-dot infrared photodetector. *IEEE journal of quantum electronics, 41*(7), 974-979. DOI: http://dx.doi.org/10.1109/JQE.2005.848901
18. Xu, W., Liu, W., Schmidt, J. F., Zhao, W., Lu, X., Raab, T., Diederichs, C., Gao, W., Seletskiy, D. V., & Xiong Q. (2017). Correlated fluorescence blinking in two-dimensional semiconductor heterostructures. *Nature, 541*(7635), 62-67. DOI: https://doi.org/10.1038/nature20601
19. Shin, D. H., & Choi, S. H. (2018). Graphene-based semiconductor heterostructures for photodetectors. *Micromachines, 9*(7), 350. DOI: https://doi.org/10.3390/mi9070350
20. Spies, M., & Monroy, E. (2019). Nanowire photodetectors based on wurtzite semiconductor heterostructures. *Semiconductor Science and Technology, 34*(5), 053002. DOI: https://doi.org/10.1088/1361-6641/ab0cb8
21. Li, D., Chen, Y., Tang, Y., Liang, K., Ren, H., Li, F., Wang, Y., Liu, G., Song, C., Meng, L. & Zhu, B. (2023). Solution-processed organic–inorganic semiconductor heterostructures for advanced hybrid phototransistors. *ACS Applied Electronic Materials, 5*(2), 578-592. DOI: http://dx.doi.org/10.1021/acsaelm.2c01218
22. Duy Khang, N. H., & Hai, P. N. (2019). Giant unidirectional spin Hall magnetoresistance in topological insulator–ferromagnetic semiconductor heterostructures. *Journal of Applied Physics, 126*(23). DOI: http://dx.doi.org/10.48550/arXiv.1911.00247
23. Xue, F., Zhang, Y., Zhang, Y., Liao, L., Li, L., Ruan, H., Sun, L., Dong, J., Tang, C., Yu, G., Yang, Y. & Kou, X. (2021). Narrow-band semiconductor heterostructures for efficient spintronic memory device applications. In 2021 IEEE International Electron Devices Meeting (IEDM), pp. 32-5. DOI: http://dx.doi.org/10.1109/IEDM19574.2021.9720593
24. Mendez, E. E., Wang, W., Ricco, B., & Esaki, L. (1985). Resonant tunneling of holes in AlAs-GaAs-AlAs heterostructures. *Applied physics letters, 47*(4), 415-417. DOI: https://doi.org/10.1063/1.96130
25. Mendez, E. E., Esaki, L., & Wang, W. I. (1986). Resonant magnetotunneling in GaAlAs-GaAs-GaAlAs heterostructures. *Physical Review B, 33*(4), 2893. https://journals.aps.org/prb/abstract/10.1103/PhysRevB.33.2893
26. Alexander, M. G. W., Nido, M., Rühle, W. W., & Köhler, K. (1990). Resonant-tunneling transfer times between asymmetric GaAs/Al 0.35 Ga 0.65 As double quantum wells. *Physical Review B, 41*(17), 12295. https://journals.aps.org/prb/abstract/10.1103/PhysRevB.41.12295

27. Mishchenko, A., Tu, J. S., Cao, Y., Gorbachev, R. V., Wallbank, J. R., Greenaway, M. T., Morozov, V. E., Morozov, S. V., Zhu, M. J., Wong, S. L., Withers, F., Woods, C. R., Kim, Y. J., Watanabe, K., Taniguchi, T., Vdovin, E. E., Makarovsky, O., Fromhold, T. M., Fal'ko, V. I., …. Novoselov, K. S. (2014). Twist-controlled resonant tunnelling in graphene/boron nitride/graphene heterostructures. *Nature nanotechnology, 9*(10), 808-813. DOI: https://doi.org/10.1038/nnano.2014.187
28. Lin, Y. C., Ghosh, R. K., Addou, R., Lu, N., Eichfeld, S. M., Zhu, H., Li, M. Y., Peng, X., Kim, M. J., Li, L. J., Wallace, R. M., Datta, S., & Robinson, J. A. (2015). Atomically thin resonant tunnel diodes built from synthetic van der Waals heterostructures. *Nature communications, 6*(1), 7311. DOI: https://doi.org/10.1038/ncomms8311
29. Bahder, T. B., MORRISON, C. A., & BRUNO, J. D. (1987). Resonant level lifetime in GaAs/AlGaAs double-barrier structures. *Applied physics letters, 51*(14), 1089. DOI: https://doi.org/10.1063/1.98749
30. Elabsy, A. M. (2000). Effective mass dependence of resonant quasi-level lifetime in GaAs–AlxGa1− xAs double-barrier structures. Physica B: Condensed Matter, 292(3-4), 233-237. DOI: https://doi.org/10.1016/S0921-4526(00)00472-5
31. Djelti, R., Bentata, S., Aziz, Z., & Besbes, A. (2014). Effect of correlated mixed disorder on miniband structure and resonance energy of GaAs/AlxGa1-xAs superlattices. *Materials Science and Condensed Matter Physics*, 209-209. https://ibn.idsi.md/ro/vizualizare_articol/73528
32. Sattari, F. (2015). Calculation of current density for graphene superlattice in a constant electric field. *Journal of Theoretical and Applied Physics, 9*(1), 81-87. https://link.springer.com/article/10.1007/s40094-015-0165-9
33. Rebey, A., Mbarki, M., Rebei, H., & Messaoudi, S. (2022). Tunneling in matched AlGaAs/GaAsBiN superlattices. *Applied Physics A, 128*(5), 413. DOI: http://dx.doi.org/10.1007/s00339-022-05513-0
34. Elabsy, A. M., & Attia, M. T. (2023). Resonant tunneling of electrons in biased symmetric triangular double barrier nanostructure triodes. *Physica Scripta, 98*(10), 105920. http://dx.doi.org/10.1088/1402-4896/acf4d1
35. Sa-yakanit, V., & Slavcheva, G. (1998). Path-integral approach to the electron density of states at the interface of a single modulation-doped heterojunction. *Physical Review B, 58*(20), 13734. https://journals.aps.org/prb/abstract/10.1103/PhysRevB.58.13734
36. Bellucci, S., & Onorato, P. (2010). Single spin-qubit rotators based on nanojunctions: A semiclassical path integral approach. *Physica E: Low-dimensional Systems and Nanostructures, 42*(5), 1571-1578. DOI: https://doi.org/10.1016/j.physe.2009.12.047
37. Douvropoulos, T. G. (2014). Quantum Transmission via Resonant Tunneling in a Double Barrier Structure: a Path Integral Approach. *NAUSIVIOS CHORA*, 5, 15-32. https://nausivios.hna.gr/docs/2014C2.pdf
38. Hanson G. W. (2009). Fundamentals of Nanoelectronics. Pearson.https://www.amazon.in/Fundamentals-Nanoelectronics-1e-Hanson/dp/8131726797
39. Pereyra, P. (2019). Why the effective-mass approximation works so well for nano-structures. *Europhysics Letters, 125*(2), 27003. https://iopscience.iop.org/article/10.1209/0295-5075/125/27003/meta
40. Adachi, S. (1985). GaAs, AlAs, and Al x Ga1− x As: Material parameters for use in research and device applications. *Journal of applied physics, 58*(3), R1-R29. DOI: https://doi.org/10.1063/1.336070
41. Wang, Y., Zahid, F., Zhu, Y., Liu, L., Wang, J., & Guo, H. (2013). Band offset of GaAs/AlxGa1− xAs heterojunctions from atomistic first principles. *Applied Physics Letters, 102*(13). DOI: http://dx.doi.org/10.1109/EDSSC.2013.6628136
42. Meghoufel, F. Z., Bentata, S., Terkhi, S., Bendahma, F., & Cherid, S. (2013). Electronic transmission in non-linear potential profile of GaAs/AlxGa1− xAs biased quantum well structure. *Superlattices and Microstructures,* 57, 115-122. DOI: https://doi.org/10.1016/j.spmi.2013.02.008
43. Farnam, B., Solaimani, M., & Aleomraninejad, S. M. A. (2019). Effect of electron–electron interactions on optical properties of GaN/AlN quantum wells: a nonlinear Schrödinger equation approach. *Optical and Quantum Electronics, 51*(7), 218. DOI: https://link.springer.com/article/10.1007/s11082-019-1919-4
44. Gutzwiller, M. C. (1971). Periodic orbits and classical quantization conditions. *Journal of Mathematical Physics, 12*(3), 343-358. DOI: https://doi.org/10.1063/1.1665596
45. Holstein, B. R., & Swift, A. R. (1982). Barrier penetration via path integrals. *American Journal of Physics, 50*(9), 833-839. DOI: https://doi.org/10.1119/1.12751
46. Douvropoulos, T. G., & Nicolaides, C. A. (2003). Tunneling dissociation from a double well via path integrals. *The Journal of chemical physics, 119*(16), 8235-8249. DOI: http://dx.doi.org/10.1063/1.1612482
47. Terkhi, S., Bentata, S., Djelti, R., & Bouadjemi, B. (2012). Electronic transmission in random trimer InAs/InxGa1− xAs superlattices. *Results in Physics*, 2, 198-202. DOI: https://doi.org/10.1016/j.rinp.2012.10.006
48. Wang, H., Xu, H., & Zhang, Y. (2006). A theoretical study of resonant tunneling characteristics in triangular double-barrier diodes. *Physics Letters A, 355*(6), 481-488. DOI: http://dx.doi.org/10.1016/j.physleta.2006.04.007